Tracking Control of Docking Maneuvers for a Fully-Actuated Surface Vessel using Backstepping

Leticia Mayumi Kinjo, Tomas Ménard, Stefan Wirtensohn, Olivier Gehan, Johannes Reuter

Tracking Control of Docking Maneuvers for a Fully-Actuated Surface Vessel using Backstepping

Leticia Mayumi Kinjo*, Tomas Ménard*, Stefan Wirtensohn**, Olivier Gehan*, Johannes Reuter**

***Abstract*—In this paper, trajectory tracking for a fully-actuated surface vessel while performing automated docking is addressed. Environmental disturbances, integral action, as well as physical actuator quantities are directly integrated into the approach, avoiding the need for additional control allocation. By employing a backstepping design, uniform local exponential stability is proven. The performance of the controller is demonstrated by full-scale experiments. Moreover, a comparison between the physical experiments and simulations is provided.**

***Index Terms*—Trajectory tracking, Autonomous vessel, Backstepping control**

I. Introduction

In recent decades, autonomous surface vessels (ASV) have become more relevant since they are a suitable solution for important marine operations such as environmental monitoring of harsh areas where manned vessels cannot reach, coastal defense, search and rescue activities and seaborne trade [1], which has surpassed 10 billion tons of all cargoes since 2015 [2]. One of the most important fields of research to develop an ASV is vessel motion control, in which the main objective is to design a controller to solve a specific motion problem, guaranteeing that the ASV will be able to perform the demanded maneuvers accurately and safely.

One of the most popular control problems for ASV, besides the dynamic positioning [3]–[6] and the path following [7]–[10] is the trajectory tracking problem in which the controller calculates the necessary forces that the ASV needs to produce in order to track a time-varying reference trajectory. The design of the controller to solve the trajectory tracking problem was proposed in several works using different techniques such as sliding mode control [11]–[14], adaptive control [15], [16], nonlinear PID [17], and model predictive control [18]–[21]. Among these well-established control methods, the backstepping control has stood out due to its ability to guarantee stability, by obtaining the Lyapunov function with the control law and handling the nonlinearities of the vessel's dynamic model. Hence, it is also a powerful technique to design the controller for ASVs.

The backstepping technique was first implemented to solve the trajectory tracking problem for vessels in [22], where the controller, whose control law relies on the assumption that the surge velocity is always positive, was designed for an underactuated surface vessel to track optimal reference trajectories calculated using splines. An extension of the previous contribution was done later in [23] by taking into account the forces of the actuators in all three degrees of freedom (DOF), i.e. surge, sway, and yaw directions, to develop the control law using the backstepping method, showing that the controller was able to track a variety of reference trajectories.

In [24], a robust backstepping controller was developed for a fully-actuated surface vessel to address the pose tracking problem considering time-varying disturbances. In order to compensate for the disturbances' effects, an observer was designed and integrated with the controller. This combination has proved to solve the tracking problem for an arbitrary reference trajectory in simulation. Besides, in [25], the backstepping design has also considered a disturbance observer, which estimates unknown disturbances in finite time, and the first-order Levant differentiator, which calculates the virtual controls' derivatives, avoiding the singularity phenomenon.

Despite the important outcomes of the aforementioned works to solve the tracking problem employing the backstepping technique, most of them have considered the general forces as inputs, which are usually hard to measure in practice. Other works assume an affine input with linear actuator dynamics [26]. Moreover, there is a lack of experimental validation of the controllers using a real-scaled vessel. Therefore, the main contributions of this work consist of providing experimental results for a real-scaled surface vessel performing docking maneuvers using a backstepping controller, first implemented in [27], for which the complete proof of uniform local exponential stability is thoroughly developed in this paper. While the proposed method takes full advantage of the fully actuated configuration, it does not depend on the specific topology. E.g. a setup having fixed propeller and a rudder, together with a bow-thruster could be handled without modification.

The content of this paper is organized as follows. In Section II, the dynamic model of Solgenia is provided. Then, in Section III, the backstepping controller is developed and the uniform local exponential stability proof is given. The comparison of the controller's performance in simulation and real-time tests on Solgenia are assessed in Section IV. Finally, the conclusion and future work are given in Section V.

II. USV Dynamic Model

Vessels experience motion in six DOF (surge, sway, heave, yaw, roll, and pitch). Two coordinate frames are used to describe these movements, the East-North-Up (ENU) frame

*Laboratory of System Engineering, UNICAEN, ENSICAEN, 6 Bd du Marechal Juin, 14050 Caen Cedex, France (e-mail: {leticia.kinjo, tomas.menard, olivier.gehan}@ensicaen.fr).

**Institute of System Dynamics, University of Applied Sciences Konstanz, Konstanz, Germany (e-mail:{lkinjo, stwirten, jreuter}@htwg-konstanz.de)

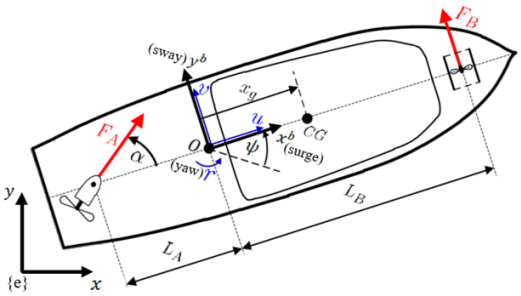

Fig. 1. Coordinate systems and actuators configuration of Solgenia

$e = (x_e, y_e, z_e)$, which is considered as an inertial frame, and the body-fixed frame $b = (x_b, y_b, z_b)$ as shown in Figure 1. In order to design a horizontal motion controller, roll, pitch, and heave are neglected and the simplified 3 DOF model is employed to represent the vessel's dynamics as in [28]

$$\dot{\boldsymbol{\eta}} = \boldsymbol{R}(\psi)\boldsymbol{\nu} \tag{1}$$

$$\boldsymbol{M}\dot{\boldsymbol{\nu}} + \boldsymbol{C}_{RB}(\boldsymbol{\nu})\boldsymbol{\nu} + \boldsymbol{N}\boldsymbol{\nu} = \boldsymbol{\tau}(n_A, \alpha, n_B) + \boldsymbol{\tau_d} \tag{2}$$

where $\boldsymbol{\eta} = [x, y, \psi]^T$ represents the position and heading angle of the vessel in $\{e\}$, and the velocities in $\{b\}$ are given by $\boldsymbol{\nu} = [u, v, r]^T$. Moreover, $\boldsymbol{\tau_d}$ denotes the disturbance forces due to the environment that are estimated by an unscented Kalman filter (UKF) which was thoroughly developed in [29]. The propulsion system of Solgenia is composed of an azimuth thruster in the back, which can turn 360° with a maximum panning rate given in Table I, and a bow thruster in the front as depicted in Figure 1. Since the thruster allocation problem is considered, the expression of $\boldsymbol{\tau}$ is given by

$$\boldsymbol{\tau} = \begin{pmatrix} F_A(n_A)\cos(\alpha) \\ F_A(n_A)\sin(\alpha) + F_B(n_B) \\ F_B(n_B)L_B - F_A(n_A)\sin(\alpha)L_A \end{pmatrix} \tag{3}$$

where L_A and L_B are the distances between the origin of the body-fixed frame and the position of the azimuth and bow thruster respectively as shown in Figure 1. It is important to highlight that $\boldsymbol{\tau}$ is not injective, which comes from the fact that each force F_A can be generated by two different configurations of the azimuth thruster. The forces of the thrusters F_A and F_B are defined as

$$F_i = p_i * n_i * |n_i|, \; i = \{A, B\} \tag{4}$$

where n_A is the rotational speed of the azimuth thruster and the constant p_A can assume two values: if $n_A \geq 0$ then $p_A = a_1 = 0.9047$, otherwise $p_A = a_2 = 0.6545$. The bow thruster velocity is given by n_B and the constant p_B can also assume two values: if $n_B \geq 0$ then $p_B = d_1 = 0.0461$, otherwise $p_B = d_2 = 0.0548$. The constant values a_1, a_2, d_1 and d_2 were obtained during the identification process as explained in [21]. Therefore, the thrusters' forces $\boldsymbol{\tau}(n_A, \alpha, n_B)$ depend on the values of the thrusters' velocities and angle, which are considered as the physical inputs, and are constrained by physical conditions of the thrusters given by

$$\begin{aligned} n_{\text{AMin}} \leq n_A \leq n_{\text{AMax}} \qquad & |\dot{\alpha}| \leq \dot{\alpha}_{\text{Max}} \\ \dot{n}_{\text{AMin}} \leq \dot{n}_A \leq \dot{n}_{\text{AMax}} \quad & n_{\text{BMin}} \leq n_B \leq n_{\text{BMax}} \end{aligned} \tag{5}$$

where n_{AMax}, n_{AMin}, $\dot{n}_{\text{AMax}}$, $\dot{n}_{\text{AMin}}$, n_{BMax}, n_{BMin}, and $\dot{\alpha}_{\text{Max}}$, denote the upper and lower bounds for azimuth thruster's velocity and acceleration, bow thruster's velocity, and azimuth thruster's panning rate respectively, and their values are given in Table I. The kinematic equation (1)

TABLE I
CONSTRAINTS.

n_{AMin}	-33.33Hz	$\dot{n}_{\text{AMin}}$	$-75\frac{\text{Hz}}{\text{s}}$
n_{AMax}	33.33Hz	$\dot{n}_{\text{AMax}}$	$75\frac{\text{Hz}}{\text{s}}$
n_{BMin}	-66.67Hz	$\dot{\alpha}_{\text{Max}}$	$1.48\frac{\text{rad}}{\text{s}}$
n_{BMax}	66.67Hz		

converts the velocities from the body-fixed frame to the inertial frame using the rotation matrix given by

$$\mathbf{R}(\psi) = \begin{pmatrix} \cos(\psi) & -\sin(\psi) & 0 \\ \sin(\psi) & \cos(\psi) & 0 \\ 0 & 0 & 1 \end{pmatrix} \tag{6}$$

where $\boldsymbol{R}^{-1}(\psi) = \boldsymbol{R}^T(\psi)$ and its derivative is given by

$$\begin{aligned} \frac{d}{dt}(\boldsymbol{R}(\psi)) &= \frac{\partial \boldsymbol{R}(\psi)}{\partial \psi}\dot{\psi} = \begin{bmatrix} -r\sin\psi & -r\cos\psi & 0 \\ r\cos\psi & -r\sin\psi & 0 \\ 0 & 0 & 0 \end{bmatrix} \\ &= \begin{bmatrix} \cos\psi & -\sin\psi & 0 \\ \sin\psi & \cos\psi & 0 \\ 0 & 0 & 1 \end{bmatrix} \begin{bmatrix} 0 & -r & 0 \\ r & 0 & 0 \\ 0 & 0 & 0 \end{bmatrix} = \boldsymbol{R}(\psi)\boldsymbol{S}(r) \end{aligned} \tag{7}$$

correspondingly, $\frac{d}{dt}(\boldsymbol{R}^T(\psi)) = -\boldsymbol{S}(r)\boldsymbol{R}(\psi)^T$. While the kinetics equation (2) depends on the mass matrix $\boldsymbol{M}$, the Coriolis and centripetal matrix $\boldsymbol{C}_{RB}(\boldsymbol{\nu})$ and the damping matrix $\boldsymbol{N}$ which are detailed in [30].

III. Backstepping Control Design

The backstepping controller is conceived in this section to address the trajectory tracking problem for the fully-actuated vessel Solgenia, whose dynamic model was detailed in Section II. The extended control model considered in this work is the same as in [30], and it will be presented here for the sake of completeness:

$$\begin{aligned} \dot{\boldsymbol{\eta}} &= \boldsymbol{R}(\psi)\boldsymbol{\nu} \\ \dot{\boldsymbol{\nu}} &= \boldsymbol{M}^{-1}(\boldsymbol{\tau}(\boldsymbol{f}) + \boldsymbol{\tau_d} - \boldsymbol{C}_{RB}(\boldsymbol{\nu})\boldsymbol{\nu} - \boldsymbol{N}\boldsymbol{\nu}) \\ \dot{\boldsymbol{f}} &= \boldsymbol{\mu} \end{aligned} \tag{8}$$

where the vector $\boldsymbol{\mu}$ contains the first derivatives of the physical inputs and represents the virtual input vector, while $\boldsymbol{f} = (n_A, \alpha, n_B)^T$. In order to design the control law using the backstepping method, first we define $\boldsymbol{f_d}$ as the necessary physical inputs to track a reference trajectory without considering the disturbances as follows:

$$\begin{aligned} \dot{\boldsymbol{\eta}}_{\boldsymbol{d}} &= \boldsymbol{R}(\psi_d)\boldsymbol{\nu_d} \\ \dot{\boldsymbol{\nu}}_{\boldsymbol{d}} &= \boldsymbol{M}^{-1}(\boldsymbol{\tau}(\boldsymbol{f_d}) - \boldsymbol{C}_{RB}(\boldsymbol{\nu_d})\boldsymbol{\nu_d} - \boldsymbol{N}\boldsymbol{\nu_d}) \end{aligned} \tag{9}$$

where $\boldsymbol{\eta_d}$ and $\boldsymbol{\nu_d}$ are the reference trajectories for the pose and the body-fixed velocities. Then, we define $\boldsymbol{f_d^p}$ as the necessary physical inputs to simultaneously track the reference and compensate for the disturbance loads and the following assumption is made:

Assumption 1. *There exists a C^1 function $\boldsymbol{f_d^p}(t)$ such that the following properties hold:*

$$\boldsymbol{\tau}(\boldsymbol{f_d^p}(t)) = \boldsymbol{\tau}(\boldsymbol{f_d}(t)) - \boldsymbol{\tau_d}(t), \quad \forall t \geq 0 \tag{10}$$

$$\boldsymbol{f_d^p}(t) \in \mathbb{U}_\xi, \quad \forall t \geq 0 \tag{11}$$

where $\mathbb{U}_\xi = \{[-n_{A_{\max}}+\xi, n_{A_{\max}}-\xi]\times(-\pi,\pi]\times[-n_{B_{\max}}+\xi, n_{B_{\max}}-\xi]\}$ *and* $\xi < min(n_{A_{\max}}, n_{B_{\max}})$.

Property (11) is used to provide a margin from the borders of the feasible input set $\mathbb{U}$, avoiding situations with unfeasible input values.

The backstepping design and its stability proof are developed in six steps. The control law is obtained in the first three steps as in [27] and they will be presented here for the sake of completeness. Then, in the fourth step, the error dynamics is reformulated using new coordinates provided by the backstepping. In the fifth step, an inequality is obtained for the remaining term in the derivative of the CLF. Finally, in the sixth step, the final inequality for the derivative of the CLF is obtained, as well as the stability proof. First, the error vectors $\boldsymbol{z_1}$, $\boldsymbol{z_2}$ and $\boldsymbol{z_3}$ are defined as

$$\boldsymbol{z_1} = \boldsymbol{\eta} - \boldsymbol{\eta_d} \tag{12}$$

$$\boldsymbol{z_2} = \boldsymbol{\nu} - \boldsymbol{\alpha_1} \tag{13}$$

$$\boldsymbol{z_3} = \boldsymbol{f} - \boldsymbol{\alpha_2} \tag{14}$$

where $\boldsymbol{\alpha_1}$, and $\boldsymbol{\alpha_2}$ are stabilizing vector-valued functions, and the reference trajectories for the pose states are given by $\boldsymbol{\eta_d}$.

Step 1: Choosing the following Lyapunov function candidate

$$V_1 = \frac{1}{2}\boldsymbol{z_1}^T\boldsymbol{z_1} \tag{15}$$

the time derivative of V_1 is given by

$$\dot{V}_1 = \boldsymbol{z_1}^T\dot{\boldsymbol{z}}_{\boldsymbol{1}} \tag{16}$$

The derivative of $\boldsymbol{z_1}$ is expressed as follows

$$\dot{\boldsymbol{z}}_{\boldsymbol{1}} = \dot{\boldsymbol{\eta}} - \dot{\boldsymbol{\eta}}_{\boldsymbol{d}} = \boldsymbol{R}(\psi)\boldsymbol{\nu} - \dot{\boldsymbol{\eta}}_{\boldsymbol{d}} = \boldsymbol{R}(\psi)(\boldsymbol{z_2} + \boldsymbol{\alpha_1}) - \dot{\boldsymbol{\eta}}_{\boldsymbol{d}} \tag{17}$$

Then, substituting (17) into (16) yields

$$\dot{V}_1 = \boldsymbol{z_1}^T[\boldsymbol{R}(\psi)\boldsymbol{z_2} + \boldsymbol{R}(\psi)\boldsymbol{\alpha_1} - \dot{\boldsymbol{\eta}}_{\boldsymbol{d}}] \tag{18}$$

The stabilization function is chosen as

$$\boldsymbol{\alpha_1} = \boldsymbol{R}^{-1}(\psi)(\dot{\boldsymbol{\eta}}_{\boldsymbol{d}} - \boldsymbol{K_1}\boldsymbol{z_1}) \tag{19}$$

where $\boldsymbol{K_1} = \boldsymbol{K_1}^T > 0$ is a control gain matrix used to tune the controller. Replacing (19) into (18) yields

$$\dot{V}_1 = -\boldsymbol{z_1}^T\boldsymbol{K_1}\boldsymbol{z_1} + \boldsymbol{z_1}^T\boldsymbol{R}(\psi)\boldsymbol{z_2} \tag{20}$$

The term $\boldsymbol{z_1}^T\boldsymbol{R}(\psi)\boldsymbol{z_2}$ will be canceled in the next step.

Step 2: Choosing the Lyapunov function candidate as

$$V_2 = V_1 + \frac{1}{2}\boldsymbol{z_2}^T\boldsymbol{M}\boldsymbol{z_2} \tag{21}$$

The time derivative of V_2 is given by

$$\dot{V}_2 = \dot{V}_1 + \boldsymbol{z_2}^T\boldsymbol{M}\dot{\boldsymbol{z}}_{\boldsymbol{2}} \tag{22}$$

From (13), the expression of $\dot{\boldsymbol{z}}_{\boldsymbol{2}}$ results in

$$\begin{aligned}\dot{\boldsymbol{z}}_{\boldsymbol{2}} =& \dot{\boldsymbol{\nu}} - \dot{\boldsymbol{\alpha}}_{\boldsymbol{1}} \\ =& \boldsymbol{M}^{-1}(-\boldsymbol{C}_{RB}(\boldsymbol{\nu})\boldsymbol{\nu} - \boldsymbol{N}\boldsymbol{\nu} + \boldsymbol{\tau}(\boldsymbol{f}) + \boldsymbol{\tau_d} - \boldsymbol{M}\dot{\boldsymbol{\alpha}}_{\boldsymbol{1}})\end{aligned} \tag{23}$$

where the time derivative of $\boldsymbol{\alpha_1}$ is given by

$$\begin{aligned}\dot{\boldsymbol{\alpha}}_{\boldsymbol{1}} = \left(\frac{d}{dt}(\boldsymbol{R}^{-1}(\psi))\right)[-\boldsymbol{K_1}(\boldsymbol{\eta} - \boldsymbol{\eta_d}) + \dot{\boldsymbol{\eta}}_{\boldsymbol{d}}] \\ + \boldsymbol{R}^{-1}(\psi)[-\boldsymbol{K_1}(\dot{\boldsymbol{\eta}} - \dot{\boldsymbol{\eta}}_{\boldsymbol{d}}) + \ddot{\boldsymbol{\eta}}_{\boldsymbol{d}}]\end{aligned} \tag{24}$$

Replacing (23) and (20) into (22), we have

$$\begin{aligned}\dot{V}_2 =& -\boldsymbol{z_1}^T\boldsymbol{K_1}\boldsymbol{z_1} + \boldsymbol{z_1}^T\boldsymbol{R}(\psi)\boldsymbol{z_2} \\ &+ \boldsymbol{z_2}^T(-\boldsymbol{C}_{RB}(\boldsymbol{\nu})\boldsymbol{\nu} - \boldsymbol{N}\boldsymbol{\nu} + \boldsymbol{\tau}(\boldsymbol{f}) + \boldsymbol{\tau_d} - \boldsymbol{M}\dot{\boldsymbol{\alpha}}_{\boldsymbol{1}})\end{aligned} \tag{25}$$

Choosing $\boldsymbol{\alpha_2}$ such as

$$\boldsymbol{\tau}(\boldsymbol{\alpha_2}) = \boldsymbol{C}_{RB}(\boldsymbol{\nu})\boldsymbol{\nu} + \boldsymbol{N}\boldsymbol{\nu} + \boldsymbol{M}\dot{\boldsymbol{\alpha}}_{\boldsymbol{1}} - \boldsymbol{\tau_d} - \boldsymbol{K_2}\boldsymbol{z_2} - \boldsymbol{R}^T(\psi)\boldsymbol{z_1} \tag{26}$$

where $\boldsymbol{K_2}$ is a gain matrix which $\boldsymbol{K_2} = \boldsymbol{K_2}^T > 0$. The resulting expression of $\dot{V}_2$ is given by

$$\dot{V}_2 = -\boldsymbol{z_1}^T\boldsymbol{K_1}\boldsymbol{z_1} - \boldsymbol{z_2}^T\boldsymbol{K_2}\boldsymbol{z_2} + \boldsymbol{z_2}^T(\boldsymbol{\tau}(\boldsymbol{f}) - \boldsymbol{\tau}(\boldsymbol{\alpha_2})) \tag{27}$$

In the next steps, it will be necessary to find upper bounds for the term $\boldsymbol{z_2}^T(\boldsymbol{\tau}(\boldsymbol{f}) - \boldsymbol{\tau}(\boldsymbol{\alpha_2}))$ to be able to prove uniform local exponential stability.

Step 3: Choosing the augmented Lyapunov function as

$$V_3 = V_2 + \frac{1}{2}\boldsymbol{z_3}^T\boldsymbol{z_3} \tag{28}$$

the time derivative of (28) is expressed as

$$\dot{V}_3 = \dot{V}_2 + \boldsymbol{z_3}^T\dot{\boldsymbol{z}}_{\boldsymbol{3}} \tag{29}$$

Considering the time derivative of (14) given by

$$\begin{aligned}\dot{\boldsymbol{z}}_{\boldsymbol{3}} &= \dot{\boldsymbol{f}} - \dot{\boldsymbol{\alpha}}_{\boldsymbol{2}} \\ &= \boldsymbol{\mu} - \dot{\boldsymbol{\alpha}}_{\boldsymbol{2}}\end{aligned} \tag{30}$$

and replacing it in (29) yields

$$\begin{aligned}\dot{V}_3 = -\boldsymbol{z_1}^T\boldsymbol{K_1}\boldsymbol{z_1} - \boldsymbol{z_2}^T\boldsymbol{K_2}\boldsymbol{z_2} + \boldsymbol{z_2}^T(\boldsymbol{\tau}(\boldsymbol{f}) - \boldsymbol{\tau}(\boldsymbol{\alpha_2})) \\ + \boldsymbol{z_3}^T(\dot{\boldsymbol{f}} - \dot{\boldsymbol{\alpha}}_{\boldsymbol{2}})\end{aligned} \tag{31}$$

Designing the virtual input vector μ as

$$\mu = \dot{\boldsymbol{\alpha}}_{\boldsymbol{2}} - \boldsymbol{K_3}\boldsymbol{z_3} \tag{32}$$

where $\boldsymbol{K_3}$ is a gain matrix which $\boldsymbol{K_3} = \boldsymbol{K_3}^T > 0$, and substituting (32) into (31) yields

$$\begin{aligned}\dot{V}_3 = -\boldsymbol{z_1}^T\boldsymbol{K_1}\boldsymbol{z_1} - \boldsymbol{z_2}^T\boldsymbol{K_2}\boldsymbol{z_2} - \boldsymbol{z_3}^T\boldsymbol{K_3}\boldsymbol{z_3} \\ + \boldsymbol{z_2}^T(\boldsymbol{\tau}(\boldsymbol{f}) - \boldsymbol{\tau}(\boldsymbol{\alpha_2}))\end{aligned} \tag{33}$$

Step 4: In this step, the error dynamics is defined as follows

$$\begin{aligned}\dot{\boldsymbol{z}} &= \boldsymbol{F}(\boldsymbol{z}, t) \\ &= (F_1(\boldsymbol{z_1}, \boldsymbol{z_2}, t), F_2(\boldsymbol{z_1}, \boldsymbol{z_2}, \boldsymbol{z_3}, t), F_3(\boldsymbol{z_3}))^T\end{aligned} \tag{34}$$

with

$$F_1(\boldsymbol{z_1}, \boldsymbol{z_2}, t) = \boldsymbol{R}(z_1^\psi + \psi_d)\boldsymbol{z_2} - \boldsymbol{K_1}\boldsymbol{z_1} \tag{35}$$

$$\begin{aligned}F_2(\boldsymbol{z_1}, \boldsymbol{z_2}, \boldsymbol{z_3}, t) =& \boldsymbol{M}^{-1}(\boldsymbol{\tau}(\boldsymbol{z_3} + \boldsymbol{\alpha_2}(\boldsymbol{z_1}, \boldsymbol{z_2}, t)) \\ &-\boldsymbol{\tau}(\boldsymbol{\alpha_2}(\boldsymbol{z_1}, \boldsymbol{z_2}, t)) - \boldsymbol{K_2}\boldsymbol{z_2} \\ &-\boldsymbol{R}^{-1}(z_1^\psi + \psi_d)\boldsymbol{z_1})\end{aligned} \tag{36}$$

$$F_3(\boldsymbol{z_3}) = -\boldsymbol{K_3}\boldsymbol{z_3} \tag{37}$$

where z_1^ψ is the heading angle of $\boldsymbol{z_1} = [z_1^x, z_1^y, z_1^\psi]^T$ and ψ_d is the reference trajectory for the yaw angle. Besides, the non-autonomous character of the dynamics comes from the fact that it depends on the $\boldsymbol{\eta_d}(t)$ and their derivatives.

Step 5: Given the expression of $\dot{V}_3$ represented by (33), one

needs to find upper bounds that are negative and have their magnitudes greater than the term $\boldsymbol{z_2}^T(\boldsymbol{\tau}(\boldsymbol{f})-\boldsymbol{\tau}(\boldsymbol{\alpha_2}))$ in order to obtain a uniform local exponential convergence. First note that the following inequality holds:

$$\boldsymbol{z_2}^T(\boldsymbol{\tau}(\boldsymbol{f})-\boldsymbol{\tau}(\boldsymbol{\alpha_2})) \leq ||\boldsymbol{z_2}||\,||\boldsymbol{\tau}(\boldsymbol{f})-\boldsymbol{\tau}(\boldsymbol{\alpha_2})|| \tag{38}$$

Moreover, for the term $||\boldsymbol{\tau}(\boldsymbol{f})-\boldsymbol{\tau}(\boldsymbol{\alpha_2})||$, an inequality of the form $||\boldsymbol{\tau}(\boldsymbol{f})-\boldsymbol{\tau}(\boldsymbol{\alpha_2})|| \leq L\|\boldsymbol{f}-\boldsymbol{\alpha_2}\|$ will be obtained. Since $\boldsymbol{\tau}$ is locally Lipschitz but not globally Lipschitz, one has to show that if $\boldsymbol{z}$ is taken close enough to the origin, then for all $t \geq 0$, both $\boldsymbol{f}$ and $\boldsymbol{\alpha_2}$ belong to a compact set, taken here as the feasible set of the inputs $\mathbb{U}$.
Replacing (13) and (24) into the definition of $\boldsymbol{\tau}(\boldsymbol{\alpha_2})$ in (26) yields

$$\begin{aligned}\boldsymbol{\tau}(\boldsymbol{\alpha_2}) =&(\boldsymbol{C}_{RB}(\boldsymbol{z_2}+\boldsymbol{\alpha_1}(\boldsymbol{z_1},t))+\boldsymbol{N})(\boldsymbol{z_2}\\ &+\boldsymbol{R}^{-1}(z_1^{\psi}+\psi_d)(\dot{\boldsymbol{\eta}}_{\boldsymbol{d}}(t)-\boldsymbol{K_1}\boldsymbol{z_1}))-\boldsymbol{\tau_d}(t)-\boldsymbol{K_2}\boldsymbol{z_2}\\ &-\boldsymbol{R}^T(z_1^{\psi}+\psi_d)\boldsymbol{z_1}+\boldsymbol{M}(-\boldsymbol{S}(r)\boldsymbol{R}^T(z_1^{\psi}+\psi_d)(-\boldsymbol{K_1}\boldsymbol{z_1}\\ &+\dot{\boldsymbol{\eta}}_{\boldsymbol{d}}(t)))+\boldsymbol{M}\boldsymbol{R}^{-1}(z_1^{\psi}+\psi_d)(-\boldsymbol{K_1}\dot{\boldsymbol{z}}_{\boldsymbol{1}}+\ddot{\boldsymbol{\eta}}_{\boldsymbol{d}}(t))\\ =&\boldsymbol{h}(\boldsymbol{z_1},\boldsymbol{z_2},t)-\boldsymbol{\tau_d}(t)\end{aligned} \tag{39}$$

where $\boldsymbol{h}(\boldsymbol{z_1},\boldsymbol{z_2},t)$ is a continuous function, which verifies $h(0,0,t)=\boldsymbol{\tau}(\boldsymbol{f_d}(t))$. The forces to track a disturbed reference trajectory are defined as in (10) then, we have that

$$\forall\,\varepsilon>0\;\exists\,\delta>0 \mid \|\boldsymbol{z}\|<\delta \implies \|\boldsymbol{\tau}(\boldsymbol{\alpha_2})-\boldsymbol{\tau}(\boldsymbol{f_d^p}(t))\|<\varepsilon \tag{40}$$

As mention in Section II, $\boldsymbol{\tau}$ is not injective, therefore $\|\boldsymbol{\tau}(\boldsymbol{\alpha_2})-\boldsymbol{\tau}(\boldsymbol{f_d^p}(t))\|$ being small does not mean that $\boldsymbol{\alpha_2}$ and $\boldsymbol{f_d^p}(t)$ are close. Then, $\boldsymbol{f_d^p}(t)$ belonging to $\mathbb{U}_\xi$ does not necessarily mean that $\boldsymbol{\alpha_2}$ belongs to $\mathbb{U}$. Hence, we will show that there is a $\delta>0$ such that

$$\text{if } \boldsymbol{f_d^p}\in\mathbb{U}_\xi \text{ and } \|\boldsymbol{\tau}(\boldsymbol{f_d^p})-\boldsymbol{\tau}(\boldsymbol{\alpha_2})\|<\delta \text{ then } \boldsymbol{\alpha_2}\in\mathbb{U} \tag{41}$$

A restriction of $\boldsymbol{\tau}$ is considered as $\bar{\boldsymbol{\tau}}:(\mathbb{R}_+,(-\pi,\pi],\mathbb{R})\to\mathbb{R}^3$, which corresponds to forces generated only by a positive velocity of the azimuth thruster. Hence, proving (41) for $\bar{\boldsymbol{\tau}}$ also proves it for $\boldsymbol{\tau}$, since if an antecedent of $\bar{\boldsymbol{\tau}}$ belongs to $\mathbb{U}$, it means that the other antecedent of $\boldsymbol{\tau}$ also belongs to $\mathbb{U}$. Now, we state the following lemma:

Lemma 1. *There exists $\delta>0$ such that, if $\boldsymbol{f_1}\in\mathbb{U}_\xi$ and $\|\bar{\boldsymbol{\tau}}(\boldsymbol{f_1})-\bar{\boldsymbol{\tau}}(\boldsymbol{f_2})\|<\delta$, then $\boldsymbol{f_2}\in\mathbb{U}$.*

The proof of Lemma 1 can be found in the appendix A. Applying Lemma 1 with $\boldsymbol{f_1}=\boldsymbol{f_d^p}$ and $\boldsymbol{f_2}=\boldsymbol{\alpha_2}$, we have then proved that there exists $\delta>0$ such that, for all $t\geq 0$, and $\boldsymbol{z}\in\mathbb{R}^9$ verifying $\|\boldsymbol{z}\|<\delta$, $\boldsymbol{\alpha_2}\in\mathbb{U}$ and, consequently, $\boldsymbol{f}$ is in the neighbourhood of $\mathbb{U}$. Hence, the following inequality holds

$$||\boldsymbol{\tau}(\boldsymbol{f})-\boldsymbol{\tau}(\boldsymbol{\alpha_2})|| \leq \underbrace{\left[\sup_{\boldsymbol{f}\in\mathbb{U}}\left\|\frac{\partial\boldsymbol{\tau}}{\partial\boldsymbol{f}}(\boldsymbol{f})\right\|\right]}_{\triangleq L}||\boldsymbol{f}-\boldsymbol{\alpha_2}|| \tag{42}$$

Step 6: The goal of this final step is to prove the uniform local exponential convergence of $\boldsymbol{z}$ to zero. Let us prove that there exists an open neighborhood of the origin $H\subset\mathbb{R}^9$ such that

$$\dot{V}_3=\langle\nabla V_3(\boldsymbol{z}),\boldsymbol{F}(\boldsymbol{z},t)\rangle\leq-\chi||\boldsymbol{z}||^2,\forall\,t\geq 0\,\text{and}\,\forall\,\boldsymbol{z}\in H \tag{43}$$

with $\chi>0$ to be determined. Using inequality (42) with (38) gives

$$\boldsymbol{z_2}^T(\boldsymbol{\tau}(\boldsymbol{f})-\boldsymbol{\tau}(\boldsymbol{\alpha_2}))\leq(\gamma||\boldsymbol{z_2}||)\left(\frac{L}{\gamma}||\boldsymbol{f}-\boldsymbol{\alpha_2}||\right) \tag{44}$$

where the constant $\gamma>0$ is introduced to give more freedom in the choice of the gains $\boldsymbol{K_2}$ and $\boldsymbol{K_3}$. Applying the Cauchy-Schwarz inequality on (44), we have

$$\boldsymbol{z_2}^T(\boldsymbol{\tau}(\boldsymbol{f})-\boldsymbol{\tau}(\boldsymbol{\alpha_2}))\leq\frac{\gamma^2}{2}||\boldsymbol{z_2}||^2+\frac{1}{2}\left(\frac{L}{\gamma}\right)^2||\boldsymbol{z_3}||^2 \tag{45}$$

Using (45) in (33) yields

$$\begin{aligned}\dot{V}_3\leq&-\boldsymbol{z_1}^T\boldsymbol{K_1}\boldsymbol{z_1}-\boldsymbol{z_2}^T\left(\boldsymbol{K_2}-\frac{\gamma^2}{2}\boldsymbol{I}\right)\boldsymbol{z_2}\\ &-\boldsymbol{z_3}^T\left(\boldsymbol{K_3}-\frac{1}{2}\left(\frac{L}{\gamma}\right)^2\boldsymbol{I}\right)\boldsymbol{z_3}\end{aligned} \tag{46}$$

Using the Rayleigh quotient, we have

$$\begin{aligned}\dot{V}_3\leq&-\lambda_{min}(\boldsymbol{K_1})||\boldsymbol{z_1}||^2-\lambda_{min}\left(\boldsymbol{K_2}-\frac{\gamma^2}{2}\boldsymbol{I}\right)||\boldsymbol{z_2}||^2\\ &-\lambda_{min}\left(\boldsymbol{K_3}-\frac{1}{2}\left(\frac{L}{\gamma}\right)^2\boldsymbol{I}\right)||\boldsymbol{z_3}||^2\leq-\chi||\boldsymbol{z}||^2\end{aligned} \tag{47}$$

with $\boldsymbol{K_2}>\frac{\gamma^2}{2}\boldsymbol{I}$, $\chi=min\Bigg(\lambda_{min}(\boldsymbol{K_1}),\lambda_{min}\left(\boldsymbol{K_2}-\frac{\gamma^2}{2}\boldsymbol{I}\right),\lambda_{min}\left(\boldsymbol{K_3}-\frac{1}{2}\left(\frac{L}{\gamma}\right)^2\boldsymbol{I}\right)\Bigg)$, and $\boldsymbol{K_3}>\frac{1}{2}\left(\frac{L}{\gamma}\right)^2\boldsymbol{I}$.

Finally, applying Theorem 4.10 p.154 in [31] gives the uniform local exponential stability. It is important to notice that the thruster's constraints were not taken into account into the backstepping development. Therefore it would be possible to have impulse values for the panning rate in $\dot{\boldsymbol{\alpha}}_{\boldsymbol{2}}$, and consequently to have discontinuities on the angle α when $n_A=0$. However, even if these discontinuities appear on the inputs, the values of the forces represented by $\boldsymbol{\tau}(\boldsymbol{\alpha_2})$ remain continuous and they are not affected by the discontinuities in this case. Furthermore, the inner control loops responsible for the actuators' dynamics are considered faster than the backstepping controller, hence the discontinuities on the inputs are negligible and they do not jeopardize the tracking of the pose and the body-fixed velocities of the vessel for practical applications. As L is obtained from (42), the conditions for the gain matrices $\boldsymbol{K_2}$ and $\boldsymbol{K_3}$ are quite conservative. However, since the Lyapunov function does not rely on $\boldsymbol{K_3}$, the latter can be adapted, to prevent high gains from being applied on $\boldsymbol{\mu}$ while still guaranteeing uniform local exponential stability, by establishing the following proposition:

Proposition 1. *Consider system* (8) *with the control input vector $\boldsymbol{\mu}$ designed as in* (32) *and the candidate Lyapunov*

function given by (28). *Let* $\beta > 0$ *and the gains* $\boldsymbol{K_1}, \boldsymbol{K_2}, \boldsymbol{K_3}$ *be chosen such that* $\boldsymbol{K_1} > 0$, $\boldsymbol{K_2} > \frac{\gamma^2}{2}\boldsymbol{I}$ *and*

$$\boldsymbol{K_3} = \begin{cases} \boldsymbol{I} \text{ if } V_3 \leq \beta \\ \boldsymbol{I} \text{ if } V_3 > \beta \text{ and} \\ \quad -\boldsymbol{z_1}^T\boldsymbol{K_1}\boldsymbol{z_1} - \boldsymbol{z_2}^T\boldsymbol{K_2}\boldsymbol{z_2} - \boldsymbol{z_3}^T\boldsymbol{z_3} \\ \quad +\boldsymbol{z_2}^T(\boldsymbol{\tau(f)} - \boldsymbol{\tau(\alpha_2)}) < -\|\boldsymbol{z}\|^2 \\ \left(\frac{1}{2}\left(\frac{L}{\gamma}\right)^2 + 1\right)\boldsymbol{I} \text{ else} \end{cases}$$

Then the error system (34) *is uniformly locally stable and the set* $\{\boldsymbol{z} \in \mathbb{R}^9 \,|\, V_3(z) \leq \beta K\}$ *is globally attractive, with*

$$K = \frac{\left|\left(-1 + \left(\frac{\gamma}{L}\right)^2\right)\right|}{\min\{2\lambda_{\min}(\boldsymbol{K_1}), 2\lambda_{\min}(\boldsymbol{K_2})\lambda_{\min}(\boldsymbol{M}), 2\}} \tag{48}$$

if $\beta > 0$ *is taken sufficiently small, that is such that the set* $\{\boldsymbol{z} \in \mathbb{R}^9 \,|\, V_3(z) \leq \beta K\} \subset H$, *where* H *is a neighborhood of the origin given by* (43).

Proof. In order to obtain the stability result, let us prove that the following inequality holds:

$$\dot{V}_3 \leq -aV_3 + b \tag{49}$$

in the neighborhood H, with $b = \beta\left|\left(-1 + \left(\frac{\gamma}{L}\right)^2\right)\right|$ and $a = \min\{2\lambda_{\min}(\boldsymbol{K_1}), 2\lambda_{\min}(\boldsymbol{K_2})\lambda_{\min}(\boldsymbol{M}), 2\}$. Indeed, considering inequality (49) and using the comparison lemma from [31] we have that

$$V_3(t) \leq \frac{b}{a} + \left(V_3(0) - \frac{b}{a}\right)e^{-at} \tag{50}$$

which directly gives the result. One now proves inequality (49) for the three cases for the definition of $\boldsymbol{K_3}$. For the first case, if $V_3 \leq \beta$, consider inequality (46), then, given the assumptions of the gains $\boldsymbol{K_1}, \boldsymbol{K_2}, \boldsymbol{K_3}$, one obtains

$$\dot{V}_3(t) \leq -aV_3(t) + \frac{1}{2}\boldsymbol{z_3}^T\left(\left(1 + \left(\frac{\gamma}{L}\right)^2\right)\boldsymbol{I} - 2\boldsymbol{K_3}\right)\boldsymbol{z_3} \tag{51}$$

Since in this case $\boldsymbol{K_3} = \boldsymbol{I}$ an over-valuation of the second term on the right-hand side of (51) is given as follows

$$\begin{aligned}(\star) &\leq \left|\left(\left(1 + \left(\frac{\gamma}{L}\right)^2\right) - 2\right)\right|\frac{1}{2}\boldsymbol{z_3}^T\boldsymbol{z_3} \\ &\leq \left|\left(-1 + \left(\frac{\gamma}{L}\right)^2\right)\right| V_3 \\ &\leq \left|\left(-1 + \left(\frac{\gamma}{L}\right)^2\right)\right| \beta = b\end{aligned}$$

For the second case, $-\boldsymbol{z_1}^T\boldsymbol{K_1}\boldsymbol{z_1} - \boldsymbol{z_2}^T\boldsymbol{K_2}\boldsymbol{z_2} - \boldsymbol{z_3}^T\boldsymbol{z_3} + \boldsymbol{z_2}^T(\boldsymbol{\tau(f)} - \boldsymbol{\tau(\alpha_2)})$ is the expression of $\dot{V}_3$ when $\boldsymbol{K_3} = \boldsymbol{I}$ which directly give the inequality. For the last case, taking the expression of $\boldsymbol{K_3}$, one can directly show that the second term on the right-hand side of inequality (51) is negative, which gives the required inequality. □

IV. Experimental Results

The performance of the controller was assessed experimentally by integrating on Solgenia the backstepping controller conceived in Section III and implemented on Matlab/Simulink. Solgenia is a $8\,\mathrm{m}$-long solar boat equipped with an RTK-GPS system, which uses two Trimble (BX982) antennas, it also has rotational encoders directly in the propellers' shaft to measure their velocities and a Microautobox2 (MABX2) [32] as depicted in Figure 2. The experimental tests were done at the Rhine river, aiming to perform various docking maneuvers, calculated by a trajectory planner, first used in [29], which generates a reference trajectory between the initial position of the vessel and the university's docking spot. During the experiments, the docking maneuvers were performed consecutively with different initial poses. Once the data of the experimental tests were collected, a comparison of the performance of the backstepping controller in simulation and in real-time has been conducted. For that, the same initial poses and the estimated disturbance forces $\boldsymbol{\tau_d}$ obtained in the experimental tests were used in the simulations on Matlab. The backstepping parameters used in all of the docking maneuvers are $\boldsymbol{K_1} = \boldsymbol{I_3}$, $\boldsymbol{K_2} = diag(10^3, 10^3, 10^4)$ and $\boldsymbol{K_3}$ depends on *Proposition 1*, $\gamma = 20$, and $\dot{\boldsymbol{\alpha}}_{\boldsymbol{2}}$ was obtained by applying a differentiator associated with a second-order low-pass filter with a bandwidth of $10Hz$ on $\boldsymbol{\alpha_2}$ to filter the discontinuities that could appear in the derivative calculation. It should be noted that the bandwidth of this filter has to be chosen carefully to be greater than the bandwidth of the closed loop system. Besides, saturation blocks were used in the Simulink model to implement the thrusters' constraints listed in Table I.

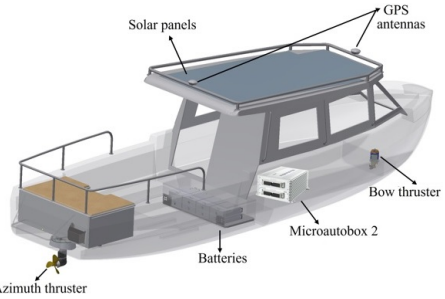

Fig. 2. Equipment of the research boat Solgenia.

The forward docking maneuver had initial pose $\boldsymbol{\eta_i} = [-10\,\mathrm{m}, 30\,\mathrm{m}, -73.23°]^T$ as depicted in Figure 3, where it can be observed that the docking maneuver was executed correctly in both cases. Furthermore, the root mean square error (RMSE) values for the simulation and the real-time test are given in Table II, showing that the experimental results presented higher tracking errors compared to the simulation ones, however, it still remains an accurate performance since the RMSE values were below $20\,\mathrm{cm}$. The states representing the body-fixed velocities were able to track their references as depicted in Figure 4, overcoming the disturbance forces. The physical inputs are illustrated in Figure 5, showing that the thrusters have respected their limits, given in Table I, not saturating in any case. Besides, in this maneuver, one can see that the thrusters can assume different configurations to generate almost the same forces that result in the same

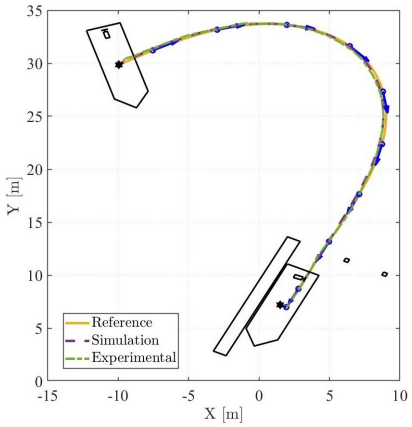

Fig. 3. XY-Plot for the forward docking maneuver.

TABLE II
RMSE VALUES FOR THE FORWARD DOCKING.

States	Experimental RMSE	Simulation RMSE
x[m]	0.1362	0.0836
y[m]	0.2037	0.0455
ψ[rad]	0.0360	0.0113
u[m/s]	0.0197	0.0084
v[m/s]	0.0236	0.0081
r[rad/s]	0.0089	0.0026

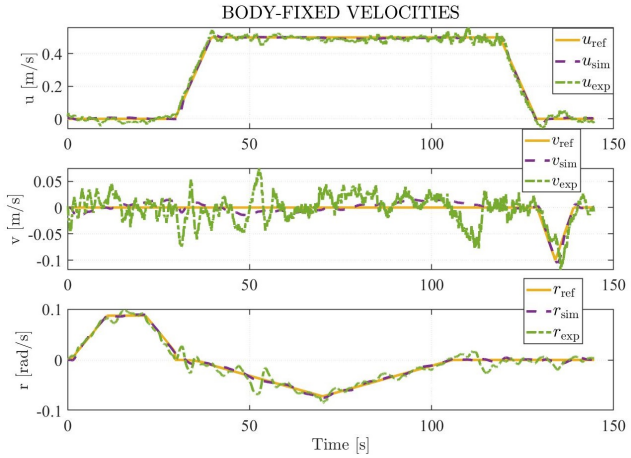

Fig. 4. Body-fixed velocity states for the forward docking maneuver.

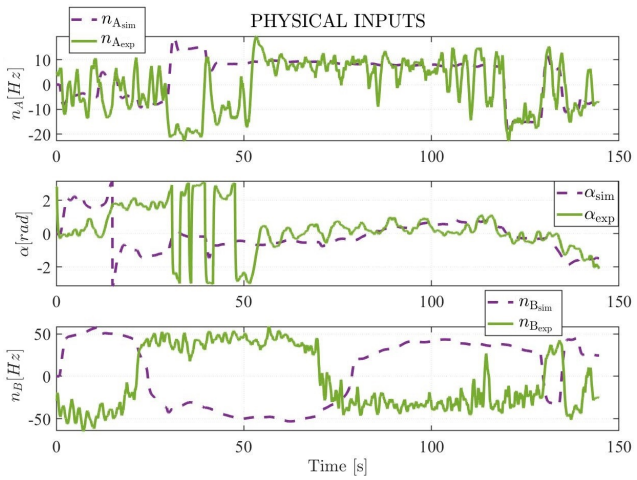

Fig. 5. Physical inputs for the forward docking maneuver.

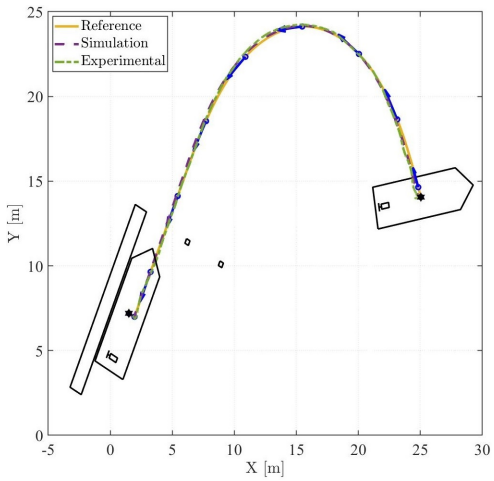

Fig. 6. XY-Plot for the backward docking maneuver.

TABLE III
RMSE VALUES FOR THE BACKWARD DOCKING MANEUVER.

States	Experimental RMSE	Simulation RMSE
x[m]	0.1991	0.0680
y[m]	0.2336	0.0827
ψ[rad]	0.0421	0.0157
u[m/s]	0.0275	0.0118
v[m/s]	0.0269	0.0137
r[rad/s]	0.0130	0.0057

movement. This difference can be observed during the first 50 s in Figure 5, where the velocity of the bow thruster n_B assumes opposite values in simulation and in the experimental test. The angle α presents the same behavior during the same period, while the azimuth thruster velocity n_A has this effect after the first 25 s. The backward docking was the other maneuver to study the performance of the controller starting with an initial pose $\boldsymbol{\eta_i} = [25\,\text{m}, 14\,\text{m}, 10.08°]^T$ as depicted in Figure 6. In this scenario, the backstepping controller was also able to perform the docking correctly with the tracking errors given in Table III, where one can see that the controller has performed better in simulation than in the experimental scenario, the latter presenting a position error slightly above 20 cm, which can still be considered as precise enough for this type of maneuver. Figure 7 depicts the body-fixed velocities tracking their reference trajectories. As the forward docking, the RMSE values of all the states show a reasonable performance for the experimental test, even if it is not as accurate as the simulation. In this scenario, the physical inputs depicted in Figure 8 have also respected the thrusters' constraints to perform the backward docking. Besides, the distinct configuration for the thrusters in simulation and in the experimental test is shown in Figure 8 as well, being more explicit during the first 20 s.

V. CONCLUSION

This paper has presented the detailed development of the backstepping controller first presented in [27], for which uniform local exponential stability has been proven, considering the thruster allocation problem and disturbances to solve the tracking problem for the fully-actuated vessel Solgenia. The real-time tests were done to execute docking maneuvers from different initial poses, resulting in a reasonable performance compared to the simulation, validating the backstepping controller. The perspective of future work is to use the Lyapunov function obtained for the backstepping controller as a con-

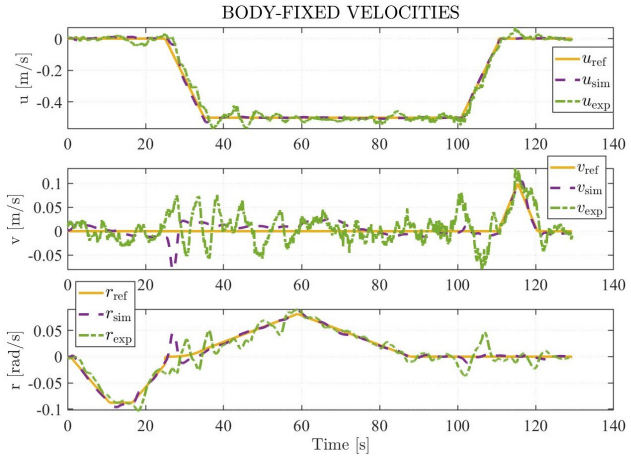

Fig. 7. Body-fixed velocity states for the backward docking maneuver.

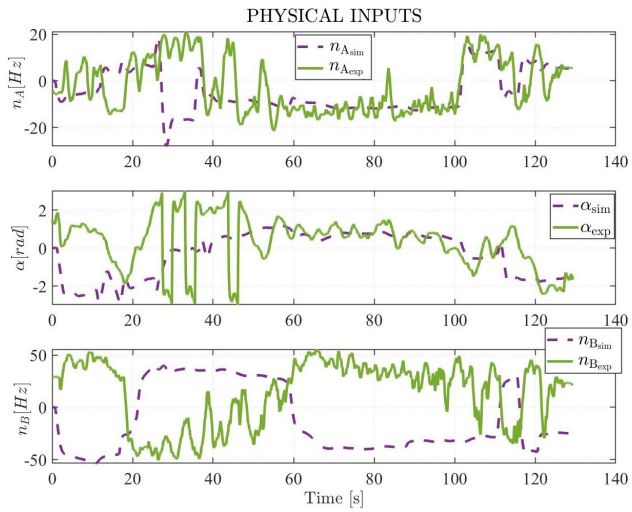

Fig. 8. Physical inputs for the backward docking maneuver.

traction constraint of a nonlinear model predictive controller to guarantee stability for it as well and test it in simulation and on Solgenia.

Appendix A
Proof of Lemma 1

The restriction $\bar{\boldsymbol{\tau}}$ is not injective, except outside of the subspace $W = \{(0, \alpha, n_B)^T \mid \alpha \in (-\pi, \pi], \; n_B \in [-n_{B_{\max}} + \xi, n_{B_{\max}} - \xi]\}$. Considering $\boldsymbol{f_1} = [n_{A1}, \alpha_1, n_{B1}]^T$ and $\boldsymbol{f_2} = [n_{A2}, \alpha_2, n_{B2}]^T$, the following lemma holds:

Lemma 2. *if* $\boldsymbol{f_1}, \boldsymbol{f_2} \notin W$ *then* $\bar{\boldsymbol{\tau}}(\boldsymbol{f_1}) = \bar{\boldsymbol{\tau}}(\boldsymbol{f_2}) \implies \boldsymbol{f_1} = \boldsymbol{f_2}$

The proof of Lemma 2 is straightforward and it can be obtained from the definition of $\boldsymbol{\tau}$ in (3). In order to prove Lemma 1, the following subspace of $\mathbb{U}$ is considered.

$$\mathbb{V}(\zeta) = \{\boldsymbol{u} \in \mathbb{U} \mid d(\boldsymbol{u}, W) \geq \zeta\} \tag{52}$$

where

$$d(\boldsymbol{u}, W) = \min_{\boldsymbol{v} \in W} \|\boldsymbol{u} - \boldsymbol{v}\| \tag{53}$$

denotes the distance between $\boldsymbol{u}$ and the set W. Then, the following two cases are considered:

Case 1: $\boldsymbol{f_1} = [n_{A1}, \alpha_1, n_{B1}]^T \notin \mathbb{V}(\zeta)$

In this case, given the definition of $\mathbb{V}(\zeta)$, there is a point $\boldsymbol{f_3} = [0, \alpha_3, n_{B3}]^T$ of the singular set W that is close to $\boldsymbol{f_1}$, indeed

$$\forall \; \boldsymbol{f_1} \notin \mathbb{V}(\zeta) \; \exists \; \boldsymbol{f_3} \in W \mid \|\boldsymbol{f_1} - \boldsymbol{f_3}\| \leq \zeta \tag{54}$$

Then, we have

$$\|\bar{\boldsymbol{\tau}}(\boldsymbol{f_3}) - \bar{\boldsymbol{\tau}}(\boldsymbol{f_2})\| \leq \|\bar{\boldsymbol{\tau}}(\boldsymbol{f_3}) - \bar{\boldsymbol{\tau}}(\boldsymbol{f_1})\| + \|\bar{\boldsymbol{\tau}}(\boldsymbol{f_1}) - \bar{\boldsymbol{\tau}}(\boldsymbol{f_2})\| \tag{55}$$

Since $\bar{\boldsymbol{\tau}}$ is Lipschitz continuous on $\mathbb{U}$ with a Lipschitz constant L, (55) can be reformulated as follows

$$\|\bar{\boldsymbol{\tau}}(\boldsymbol{f_3}) - \bar{\boldsymbol{\tau}}(\boldsymbol{f_2})\| \leq L\zeta + \delta \tag{56}$$

assuming that $\|\bar{\boldsymbol{\tau}}(\boldsymbol{f_1}) - \bar{\boldsymbol{\tau}}(\boldsymbol{f_2})\| \leq \delta$, with $\delta > 0$. Then, using the formulation of $\boldsymbol{\tau}$ as in (3), (56) can be expanded as

$$|-F_A(n_{A2}) \cos \alpha_2| \leq L\zeta + \delta \tag{57}$$

$$|-F_A(n_{A2}) \sin \alpha_2 + (F_B(n_{B3}) - F_B(n_{B2}))| \leq L\zeta + \delta \tag{58}$$

$$\left| F_A(n_{A2}) \sin \alpha_2 + \frac{L_B}{L_A}(F_B(n_{B3}) - F_B(n_{B2})) \right| \leq \frac{1}{L_A}(L\zeta + \delta) \tag{59}$$

where $L_B > L_A$. Applying the second triangle inequality in (58) and (59) yields

$$|F_A(n_{A2}) \sin \alpha_2| - |F_B(n_{B3}) - F_B(n_{B2})| \leq L\zeta + \delta \tag{60}$$

$$\frac{L_B}{L_A} |F_B(n_{B3}) - F_B(n_{B2})| - |F_A(n_{A2}) \sin \alpha_2| \leq \frac{1}{L_A}(L\zeta + \delta) \tag{61}$$

Adding (60) to (61) and denoting $p = \frac{1 + L_A}{(L_B - L_A)}$ results in

$$|F_B(n_{B3}) - F_B(n_{B2})| \leq Lp\zeta + p\delta \tag{62}$$

Now, choosing ζ and δ such that $\zeta \leq \frac{p_B \xi^2}{2Lp}$ and $\delta \leq \frac{p_B \xi^2}{2p}$. Then, using the second triangle equation, we get

$$|F_B(n_{B2})| - |F_B(n_{B3})| \leq p_B \xi$$

Therefore $|n_{B2}|^2 \leq |n_{B3}|^2 + \xi^2$. Adding $2|n_{B3}|\xi$ to the right hand side and taking the root yields $|n_{B2}| \leq |n_{B3}| + \xi \leq n_{B_{max}}$ since $\boldsymbol{f_3} \in W$.

Similarly than for equation (62), adding (L_B/L_A) times (60) to (61), squaring it and adding it to the square of (57) gives

$$|F_A(n_{A2})|^2 \leq (1 + \tilde{L}^2)(L\zeta + \delta)^2 \tag{63}$$

with $\tilde{L} = (1 + L_B)/(L_B - L_A)$. Now, choosing ζ and δ such that $\zeta \leq \frac{q p_A}{2L} \xi^2$, and $\delta \leq \frac{q p_A}{2} \xi^2$. Then, taking the square of (63) we get $|n_{A2}| \leq \xi \leq |n_{A_{max}}|$ with $q = (1 + \tilde{L}^2)^{-1/2}$. Combining the results, we get that if ζ and δ are chosen such that

$$\zeta \leq min \left\{ \frac{p_A}{2Lq} \xi^2, \frac{p_B \xi^2}{2pL} \right\} \text{ and } \delta \leq min \left\{ \frac{q_A \xi^2}{2q}, \frac{p_B \xi^2}{2p} \right\}$$

then $\boldsymbol{f_2}$ belongs to $\mathbb{U}$, which proves the lemma for the first case.

Case 2: $\boldsymbol{f_1} = [n_{A1}, \alpha_1, n_{B1}]^T \in \mathbb{V}(\zeta)$

Since $\bar{\boldsymbol{\tau}}$ is injective, as shown in Lemma 2, we want to show that for all $\varepsilon > 0$ there is a $\delta > 0$ such that

$$\forall \; \boldsymbol{f_1} \in \mathbb{V}(\zeta), \|\bar{\boldsymbol{\tau}}(\boldsymbol{f_1}) - \bar{\boldsymbol{\tau}}(\boldsymbol{f_2})\| < \delta \implies \|\boldsymbol{f_1} - \boldsymbol{f_2}\| < \varepsilon \tag{64}$$

Property (64) basically means that the inverse of $\bar{\boldsymbol{\tau}}$ is uniformly continuous on $\bar{\boldsymbol{\tau}}(\mathbb{V}(\zeta))$. In order to prove the continuity, one explicitly computes $\bar{\boldsymbol{\tau}}^{-1}$ on $\bar{\boldsymbol{\tau}}(\mathbb{V}(\zeta))$. Then, knowing that $\bar{\boldsymbol{\tau}}(n_A, \alpha, n_B) = (\bar{X}, \bar{Y}, \bar{N})^T$, the following system needs to be solved:

$$\bar{X} = F_A(n_A)\cos\alpha \tag{65}$$

$$\bar{Y} = F_A(n_A)\sin\alpha + F_B(n_B) \tag{66}$$

$$\bar{N} = L_B F_B(n_B) - L_A F_A(n_A)\sin\alpha \tag{67}$$

Multiplying (66) by $-L_A$, then adding to (67) results in

$$F_B(n_B) = \frac{L_A\bar{Y} + \bar{N}}{L_A + L_B} \tag{68}$$

In the same way, to obtain $F_A(n_A)$, (66) is multiplied by L_B, and (67) is subtracted from it. Then, elevating the resulting expression and (65) to the square and adding each other

$$F_A(n_A) = \sqrt{\bar{X}^2 + \left(\frac{L_B\bar{Y} - \bar{N}}{L_B + L_A}\right)^2} \tag{69}$$

One can obtain the expressions of n_A and n_B by replacing (68) and (69) into (4). Besides, as we are considering that $F_A(n_A) \geq \zeta$ with $\zeta > 0$, since for $\boldsymbol{u} = [n_A, \alpha, n_B]^T \in \mathbb{V}(\zeta)$, we have

$$|n_A| = \left\| \begin{pmatrix} n_A \\ \alpha \\ n_B \end{pmatrix} - \begin{pmatrix} 0 \\ \alpha \\ n_B \end{pmatrix} \right\| \geq \min_{\boldsymbol{v}\in W} \|\boldsymbol{u} - \boldsymbol{v}\| \geq \zeta \tag{70}$$

Then, one has $\alpha = \arccos\left(\frac{\bar{X}}{F_A(n_A)}\right)$. Hence, $\bar{\boldsymbol{\tau}}^{-1}$ is continuous on $\bar{\boldsymbol{\tau}}(\mathbb{V}(\zeta))$. Furthermore, since $\mathbb{V}(\zeta)$ is a compact set, $\bar{\boldsymbol{\tau}}(\mathbb{V}(\zeta))$ is also a compact set and $\bar{\boldsymbol{\tau}}^{-1}$ is uniformly continuous on $\bar{\boldsymbol{\tau}}(\mathbb{V}(\zeta))$. Therefore, the property (64) is proved.

REFERENCES

[1] Z. Liu, Y. Zhang, X. Yu, and C. Yuan, "Unmanned surface vehicles: An overview of developments and challenges," *Annual Reviews in Control*, vol. 41, pp. 71 – 93, 2016.

[2] UNCTAD, "Review of maritime transport 2021," https://unctad.org/system/files/official-document/rmt2021_en_0.pdf, 2021, accessed: 2022-06-17.

[3] A. Sørensen, "A survey of dynamic positioning control systems," *Annual Reviews in Control*, vol. 35, no. 1, pp. 123–136, 2011.

[4] M. Tomera and K. Podgórski, "Control of dynamic positioning system with disturbance observer for autonomous marine surface vessels," *Sensors*, vol. 21, no. 20, p. 6723, 2021.

[5] K. Pettersen and T. Fossen, "Underactuated dynamic positioning of a ship-experimental results," *IEEE Transactions on Control Systems Technology*, vol. 8, no. 5, pp. 856–863, 2000.

[6] H. Alfheim, K. Muggerud, M. Breivik, E. Brekke, E. Eide, and O. Engelhardtsen, "Development of a dynamic positioning system for the revolt model ship," *IFAC CAMS*, vol. 51, no. 29, 2018.

[7] L. Moreira, T. Fossen, and C. Guedes Soares, "Path following control system for a tanker ship model," *Ocean Engineering*, vol. 34, no. 14, pp. 2074–2085, 2007.

[8] Y. Fan, H. Huang, and W. Tan, "Robust adaptive path following control of an unmanned surface vessel subject to input saturation and uncertainties," *Applied Sciences*, vol. 9, no. 9, p. 1815, 2019.

[9] D. Belleter, C. Paliotta, M. Maggiore, and K. Pettersen, "Path following for underactuated marine vessels," *IFAC NOLCOS*, vol. 49, no. 18, pp. 588–593, 2016.

[10] Z. Li, J. Sun, and S. Oh, "Design, analysis and experimental validation of a robust nonlinear path following controller for marine surface vessels," *Automatica*, vol. 45, no. 7, pp. 1649–1658, 2009.

[11] J. Cheng, J. Yi, and D. Zhao, "Design of a sliding mode controller for trajectory tracking problem of marine vessels," *Iet Control Theory and Applications*, vol. 1, pp. 233–237, 2007.

[12] F. Fahimi and C. V. Kleeck, "Alternative trajectory-tracking control approach for marine surface vessels with experimental verification," *Robotica*, vol. 31, no. 1, p. 25–33, 2013.

[13] H. Ashrafiuon, K. R. Muske, L. C. McNinch, and R. A. Soltan, "Sliding-mode tracking control of surface vessels," *IEEE transactions on industrial electronics*, vol. 55, no. 11, pp. 4004–4012, 2008.

[14] A. Gonzalez-Garcia and H. Castañeda, "Guidance and control based on adaptive sliding mode strategy for a usv subject to uncertainties," *IEEE Journal of Oceanic Engineering*, vol. 46, no. 4, pp. 1144–1154, 2021.

[15] C. Liu, Z. Zou, and J. Yin, "Trajectory tracking of underactuated surface vessels based on neural network and hierarchical sliding mode," *Journal of Marine Science and Technology*, vol. 20, no. 2, pp. 322–330, 2015.

[16] G. Wen, S. S. Ge, C. L. P. Chen, F. Tu, and S. Wang, "Adaptive tracking control of surface vessel using optimized backstepping technique," *IEEE Transactions on Cybernetics*, vol. 49, no. 9, pp. 3420–3431, 2019.

[17] S. Wirtensohn, O. Hamburger, H. Homburger, L. M. Kinjo, and J. Reuter, "Comparison of advanced control strategies for automated docking," *IFAC-PapersOnLine*, vol. 54, no. 16, pp. 295–300, 2021.

[18] H. Zheng, R. R. Negenborn, and G. Lodewijks, "Trajectory tracking of autonomous vessels using model predictive control," *IFAC World Congress*, vol. 47, no. 3, pp. 8812–8818, 2014.

[19] A. Haseltalab, V. Garofano, M. van Pampus, and R. R. Negenborn, "Model predictive trajectory tracking control and thrust allocation for autonomous vessels," *IFAC World Congress*, vol. 53, no. 2, pp. 14 532–14 538, 2020.

[20] M. Abdelaal, M. Franzle, and A. Hahn, "Nonlinear model predictive control for tracking of underactuated vessels under input constraints," in *IEEE EMS*, 2015, pp. 313–318.

[21] L. M. Kinjo, S. Wirtensohn, J. Reuter, T. Menard, and O. Gehan, "Trajectory tracking of a fully-actuated surface vessel using nonlinear model predictive control," *IFAC CAMS 2021*, vol. 54, no. 16, pp. 51–56, 2021.

[22] J.-M. Godhavn, "Nonlinear tracking of underactuated surface vessels," in *IEEE CDC*, vol. 1, 1996, pp. 975–980.

[23] G. Toussaint, T. Basar, and F. Bullo, "Tracking for nonlinear underactuated surface vessels with generalized forces," in *IEEE ICCA*, 2000, pp. 355–360.

[24] Y. Yang, J. Du, H. Liu, C. Guo, and A. Abraham, "A trajectory tracking robust controller of surface vessels with disturbance uncertainties," *IEEE Transactions on Control Systems Technology*, vol. 22, no. 4, pp. 1511–1518, 2014.

[25] Y. Dai, C. Yang, S. Yu, Y. Mao, and Y. Zhao, "Finite-time trajectory tracking for marine vessel by nonsingular backstepping controller with unknown external disturbance," *IEEE Access*, vol. 7, pp. 165 897–165 907, 2019.

[26] T. Fossen and S. Berge, "Nonlinear vectorial backstepping design for global exponential tracking of marine vessels in the presence of actuator dynamics," in *IEEE CDC*, vol. 5. IEEE, 1997, pp. 4237–4242.

[27] L. M. Kinjo, T. Menard, S. Wirtensohn, O. Gehan, and J. Reuter, "Backstepping control of a fully-actuated surface vessel for tracking a docking maneuver," in *IEEE ICSC*, 2022, pp. 502–507.

[28] T. Fossen, *Handbook of Marine Craft Hydrodynamics and Motion Control*. Wiley, 2011.

[29] S. Wirtensohn, O. Hamburger, H. Homburger, L. M. Kinjo, and J. Reuter, "Comparison of advanced control strategies for automated docking," *IFAC CAMS*, vol. 54, no. 16, pp. 295–300, 2021.

[30] L. M. Kinjo, S. Wirtensohn, J. Reuter, T. Menard, and O. Gehan, "Trajectory tracking of a fully-actuated surface vessel using nonlinear model predictive control: Experimental results," in *IEEE MED*, 2022, pp. 693–698.

[31] H. Khalil, *Nonlinear Systems*, ser. Pearson Education. Prentice Hall, 2002.

[32] dSpace, "Microautobox II," 2022, [Online; accessed August 12, 2022]. [Online]. Available: https://www.dspace.com/en/inc/home/products/hw/micautob/microautobox2.cfm